# Detailed Protracted Crystallization History of Perovskite in Orapa Kimberlite

Chiranjeeb Sarkar, Craig D. Storey, and Chris J. Hawkesworth

**Abstract**

Detailed petrographic and geochemical studies of perovskites from different lithofacies of Orapa kimberlite, a typical crater facies kimberlite from Botswana, have been conducted to investigate the crystallization and paragenesis of this very important groundmass phase. We suggest that there is no universal paragenetic sequence of mineral crystallization in the groundmass of kimberlite as it depends on the magma composition, which is highly variable. Our study reveals that most of the perovskite grains in Orapa grew after the macrocrystal phases such as olivine and Cr-bearing spinel, and simultaneously with "reaction" Fe-rich and groundmass spinel from ulvöspinel-magnetite group, as suggested earlier in the literature. However, certain perovskite grains contain inclusions of phlogopite and apatite, which are generally very late-crystallizing phases in kimberlite. Some perovskite grains are also found to appear as late-crystallizing rims around partially resorbed spinel. These textural features suggest protracted perovskite crystallization over a range of P and T from an evolving kimberlite magma. Previous O isotope data have also been used to suggest that perovskite crystallization succeeded late-stage magmatic degassing. Minor and trace element concentrations of Orapa perovskites also support this longer crystallization history as the post-degassed phase perovskite contain less Nb and Zr, which have preferentially partitioned into rutile, an alteration product of early-crystallizing perovskite. Calculated oxygen fugacities from Orapa perovskites range from −5.5 NNO to −0.2 NNO, emphasizing perovskite crystallization in an evolving magmatic system. Sudden degassing, mainly $CO_2$ release, prompted a change in the oxidation state of the magma, which was recorded by the late-crystallizing perovskites as this group shows an $f(O)_2$ value much higher (−2.3 NNO to −0.2 NNO) than the rest of the perovskite grains. All different lithofacies contain perovskites of different paragenesis with varying quantities while the pyroclastic kimberlite has the maximum abundance of late-stage post-degassing phase perovskites.

C. Sarkar (✉)
Department of Earth and Atmospheric Sciences, University of Alberta, Edmonton, T6G 2E3, Canada
e-mail: chiranjeeb.sarkar@ualberta.ca

C. Sarkar
Department of Earth Sciences, University of Bristol, Bristol, BS8 1RJ, UK

C. D. Storey
School of Earth and Environmental Sciences, Burnaby Building, University of Portsmouth, Portsmouth, PO1 3QL, UK

C. J. Hawkesworth
Department of Earth Sciences, University of St. Andrews, North Street, St. Andrews, KY16 9AL, Scotland

D. G. Pearson et al. (eds.), *Proceedings of 10th International Kimberlite Conference*, Volume 1, Special Issue of the Journal of the Geological Society of India,
DOI: 10.1007/978-81-322-1170-9_13, 

Keywords
Kimberlite • Perovskite • Paragenesis • Oxygen fugacity • Degassing

## Introduction

Perovskite ($CaTiO_3$) is a common primary accessory mineral phase in kimberlites. It typically constitutes up to 10 vol. % of the kimberlitic groundmass. It is an important geochemical repository of incompatible trace elements such as Nb, Ba, Sr and rare earth elements (REE) in kimberlitic magma (Mitchell 1972; Boctor and Boyd 1980; Jones and Wyllie 1984; Chakhmouradian and Mitchell 2000; Armstrong et al. 2004). Although most kimberlitic perovskite is stoichiometrically close to pure $CaTiO_3$, Nb and REE oxides can contain between 5 and 9 wt % (Chakhmouradian and Mitchell 2000, 2001; Ogilvie-Harris et al. 2010). Perovskite from kimberlite is generally enriched in LREE, particularly Ce, Nd and La, relative to HREE (Boctor and Boyd 1980; Jones and Wyllie 1984). There is minimal zoning in many grains. However, in "normally" zoned grains, the LREE, Th and occasionally Nb and Na decrease from core to rim, sometimes with increasing Fe (Chakhmouradian and Mitchell 2000). There is negligible variation in perovskite chemical compositions between different kimberlite bodies (Jones and Wyllie 1984; Mitchell 1986) or within same kimberlite (Boctor and Boyd 1981).

Perovskite is one of the main carriers of U and Th in kimberlitic magma. This and the fact that it crystallizes directly from the magma make perovskite a good geochronometer in kimberlite and other alkaline and undersaturated rocks (Heaman 1989; Heaman et al. 2003, 2004; Batumike et al. 2008). Perovskite has an extremely low Rb/Sr value (<0.001) and high Sr concentration (typically up to 0.3 wt %), which make it a potentially useful phase for Sr isotope studies and recording the initial Sr isotope composition of kimberlites (Heaman 1989). Such low Rb/Sr value means that the measured isotope ratio needs very small age correction (due to in situ decay of Rb) in order to determine the initial Sr isotope composition. Perovskite also contains a considerable amount of Sm (up to 2,000 ppm) and Nd (up to 1 wt %) with variable Sm/Nd ratios (Heaman 1989). Thus, perovskite is an excellent geochemical indicator of the kimberlite magma. Recently, perovskite has been used to determine more reliable isotopic signatures (Sr, Nd and Hf) of the kimberlite magma than those from the bulk-rock analyses (Paton et al. 2007; Yang et al. 2009; Wu et al. 2010). Moreover, Canil and Bellis (2007) have shown that Fe and Nb contents of perovskite can be used to calculate the oxygen fugacity of the magma during perovskite crystallization, and it can give important insight into diamond resorption and late-stage processes in kimberlite magma evolution.

In spite of the wealth of information that can be obtained from kimberlitic perovskite, it has not been studied as extensively as groundmass spinel. The temperature and pressure range over which perovskite crystallizes is poorly constrained. It has been suggested from initial textural studies that perovskite crystallizes at 800−600 °C after macrocrystal spinel (aluminous magnesian chromite), and nearly simultaneously with Fe-rich spinel (Mitchell 1986; Chakhmouradian and Mitchell 2000). It has also been argued that in most cases, perovskite crystallization ceases prior to the resorption of groundmass spinel and phlogopite crystallization (Chakhmouradian and Mitchell 2001). However, the situation can be more complex as crustal assimilation, and multiple batches of magma mixing are common in kimberlites. In addition, it has been shown that kimberlitic perovskite records a wide range of $f(O)_2$ (Canil and Bellis 2007; Ogilvie-Harris et al. 2010) and $^{87}Sr/^{86}Sr$ compositions (Malarkey et al. 2010) suggesting a complex paragenesis. In this contribution, we comment on perovskite crystallization and evolution following our detail petrographic and microanalytical studies of perovskite from Orapa A/K1 kimberlite pipe from Botswana.

## Geological Setting

The Orapa kimberlite is located in north-eastern Botswana, east of the Central Kalahari Basin. It is a cluster of ~60 pipes and dykes, among which the Orapa A/K1 diamond mine is the largest. It provides a 100–150-m thick-section of volcaniclastic deposits of two kimberlite pipes (North and South Pipe) that have coalesced near surface (Field et al. 1997). Orapa A/K1 has been dated as ca. 93 Ma old, and it has erupted through deformed Archaean basement overlain by volcanic and sedimentary rocks of the Karoo Supergroup (Permian–Triassic) (Davis 1977; Allsopp et al. 1989; Field et al. 1997, 2008). Orapa A/K1 is a typical example containing both crater and diatreme facies kimberlites. The Orapa North Pipe is filled with typical massive volcaniclastic kimberlite (MVK), and it is at a deeper level of erosion than the Orapa South pipe, which contains a stratiform sequence of volcaniclastic kimberlite (VK) overlain by a pyroclastic kimberlite (PK) unit (Field et al. 1997; Gernon et al. 2009). The Orapa North Pipe MVK is very

well mixed due to extensive fluidization. Orapa kimberlite contains abundant clasts of basement, basalts and sedimentary rocks, and it has distinct gas escape structures (Gernon et al. 2008, 2009). Samples used in this study were collected from MVK from Orapa North Pipe and from VK and PK from Orapa South pipes. Samples were selected from both mine surfaces and drill cores.

## Analytical Techniques

### Petrography and Geochemistry

Polished thin sections were prepared from selected hand specimens and were examined to identify perovskite crystals for further analysis. Back-scattered electron (BSE) images were taken using a Hitachi S-3500 N scanning electron microscope (SEM) with a 15–20 kV accelerating voltage at the University of Bristol. Concentrations of 19 major, minor and trace elements were measured in a Cameca SX100 EPMA with an accelerating voltage of 15–20 kV and emission current of 60 nA at Bristol. The counting times were 20 s for major elements, 30 s for LREEs, 60 s for Fe, Zr, Nb, Ta and 90 s for Th and U. Conventional ZAF correction was used to reduce counts into elemental abundances. The following standard reference materials were used to determine the chemical compositions: albite (Na), olivine (Mg, Si), sanidine (Al), wollastonite (Ca), ilmenite (Ti, Fe), $SrTiO_3$ (Sr), Y-glass (Y), zircon (Zr), $LiNbO_3$ (Nb), La-glass (La), Ce-glass (Ce), Pr-glass (Pr), Nd-glass (Nd), Sm-glass (Sm), galena (Pb), $ThO_2$ (Th) and $UO_2$ (U).

### Oxygen Fugacity

Oxygen fugacity was calculated using the empirical oxygen barometer calibration developed by (Bellis and Canil 2007). Based on the arguments put forward by Mitchell (2002), it can be assumed that all Fe in kimberlitic perovskite exists as $Fe^{+3}$. Thus, it is possible to determine the oxygen fugacity of the magma, in equilibrium with perovskite, by calculating the total Fe content of perovskite as Fe increasingly occurs as $Fe^{3+}$ in kimberlite melts with increasing $f(O)_2$. The Nb content at a given $f(O)_2$ also affects the Fe content of perovskite, so the empirical oxygen barometer is defined as follows:

$$\Delta\mathrm{NNO} = -[0.50(\pm 0.021) \times \mathrm{Nb} - \mathrm{Fe}(\pm 0.031) + 0.030(\pm 0.001)]/0.004(\pm 0.0002) \quad (1)$$

where Fe and Nb are in cation units per three oxygens, and uncertainties are given at the $2\sigma$ level (Bellis and Canil 2007). It is the $f(O)_2$ of the magma that determines the total Fe content of perovskite rather than the bulk Fe content of the melt (Bellis and Canil 2007).

## Results

### Petrography

Perovskite grains from Orapa kimberlite are in general similar to other perovskites reported from group I kimberlites worldwide (Chakhmouradian and Mitchell 2000). There is no obvious petrographic difference between perovskites from the Orapa North and South Pipe. It appears as major groundmass phase and comprises up to 10 vol % of the groundmass. The grains are euhedral to subhedral in shape, and grain sizes range between 20 and 60 μm (Fig. 1a–d) while occasionally bigger than 100 μm. Many grains are homogeneous although some show normal zonation with brighter cores and relatively darker rims in BSE images. Although rare, some grains in the studied perovskite suite show weak oscillatory zoning (Fig. 1c, d). Some complex zonation patterns were also observed where it appeared that more than one nucleus coexisted within the same crystal. Overall, perovskite crystals were classified into the following four parageneses; (1) discrete grains within the groundmass or matrix (Fig. 1c), (2) contained within ghost-lapilli or along grain boundaries of olivine macrocrysts and phenocrysts forming a "garland" (Fig. 1b), (3) intimate and complex intergrowths with groundmass spinel (Fig. 1f, h) (which often form an atoll rim around) and (4) as a reaction mantle around Ti bearing phase, for example, ilmenite macrocrysts (Fig. 1e). All four parageneses were observed in all three lithofacies; however, type (4) is rare in PK (Table 1). In places, perovskite also appears as a late-crystallizing rim around the Fe–Ti-rich spinel that has reacted to form titanite (sphene) around its grain boundary (Fig. 2e, f). Euhedral inclusions of serpentinized olivine and Cr spinel are common (Fig. 1a, g). As observed by others, perovskite and mica sometimes form a poikilitic texture where tiny perovskite crystals are included within a larger phlogopite grain (Chakhmouradian and Mitchell 2000). However, some Orapa perovskite crystals contain inclusions of phlogopite mica and apatite as well (Fig. 2b, h). Although rare, older relict perovskite grains can be found in the core of late growing perovskite rims (Fig. 2a). Based on their general appearance, perovskite grains from Orapa can be divided into two types. Some show grain boundary resorption, as there are rims of rutile around their grain boundary (Fig. 2c, d). These grains are often fractured and replaced by calcite and rutile that have filled the cracks. Sometimes, they are completely replaced

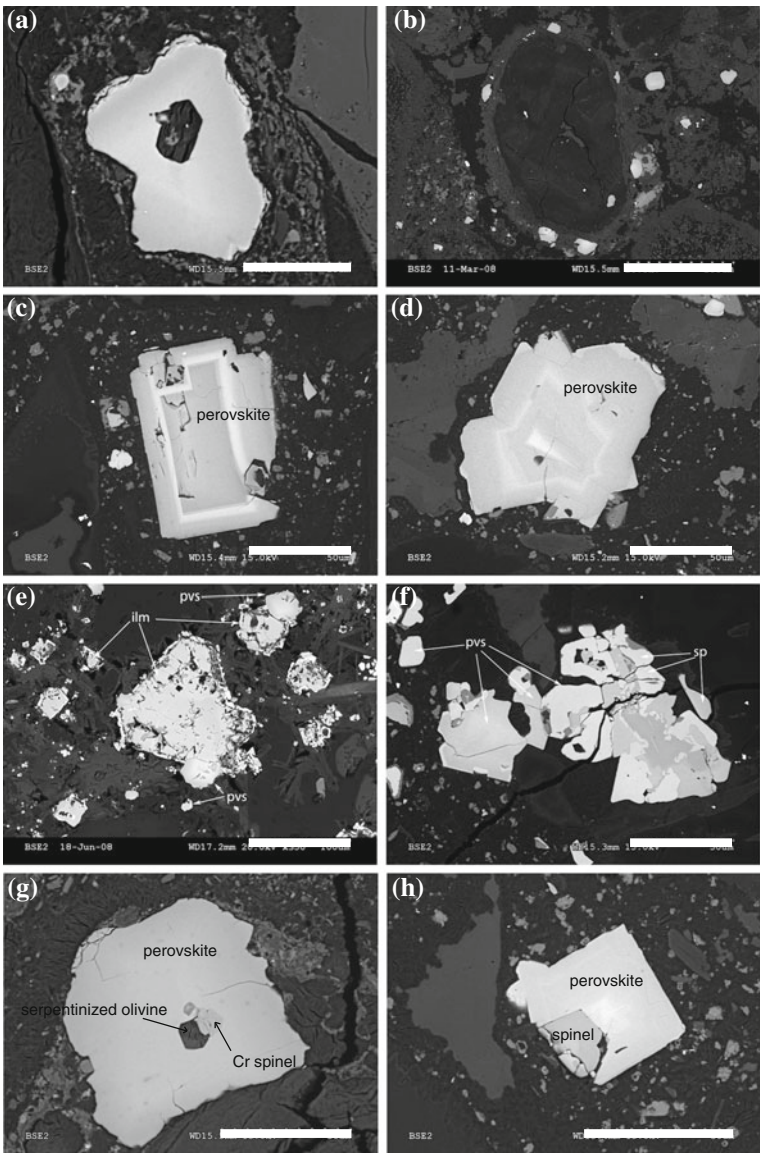


**Fig. 1** Back-scattered electron images of perovskites from Orapa. **a** Anhedral perovskite with an inclusion of euhedral serpentinized olivine. **b** Perovskite crystallizing around the grain boundary of serpentinized olivine. **c** Euhedral perovskite showing oscillatory zonation. **d** Euhedral perovskite (probably twinned) showing faint oscillatory zonation. **e** Ilmenite macrocrysts with a reaction mantle of perovskite. **f** Complex association of spinel and perovskite suggesting simultaneous growth. **g** Euhedral perovskite with inclusions of euhedral serpentinized olivine and Cr spinel. **h** Intergrowth of euhedral perovskite and spinel with straight inter-grain boundaries. (Scale bar is 50 μm in **c**, **d**, **f**, **g**, **h**; 30 μm in **a**; 300 μm in **b** and 100 μm in **e**)

**Table 1** Relative abundance of perovskites with different parageneses found in various lithofacies

| Perovskite paragenesis | | Pyroclastic kimberlite (PK) | Volcaniclastic kimberlite (VK) | Massive volcaniclastic kimberlite (MVK) |
|---|---|---|---|---|
| Major parageneses | Discrete groundmass | Abundant | Abundant | Abundant |
| | Along olivine grain boundary | Intermediate | Abundant | Abundant |
| | Intergrowth with spinel | Intermediate | Intermediate | Abundant |
| | Reaction mantle around Ilmenite | Very rare | Intermediate | Abundant |
| Minor paragenesis | Pvs with Olv and Cr spinel inclusion | Rare | Intermediate | Intermediate |
| | Pvs inclusion within phlogopite | Very rare | Rare | Rare |
| | Pvs containing inclusions of mica and apatite | Intermediate | Very rare | Rare |
| | Pvs rim around resorbed Fe–Ti spinel | Intermediate | Rare | Rare |
| Pvs with Resorbed grain boundary[a] | | Abundant | Intermediate | Intermediate |
| Fresh lozenge-shaped perovskite | | Intermediate | Intermediate | Intermediate |

[a] Denotes a secondary alteration feature

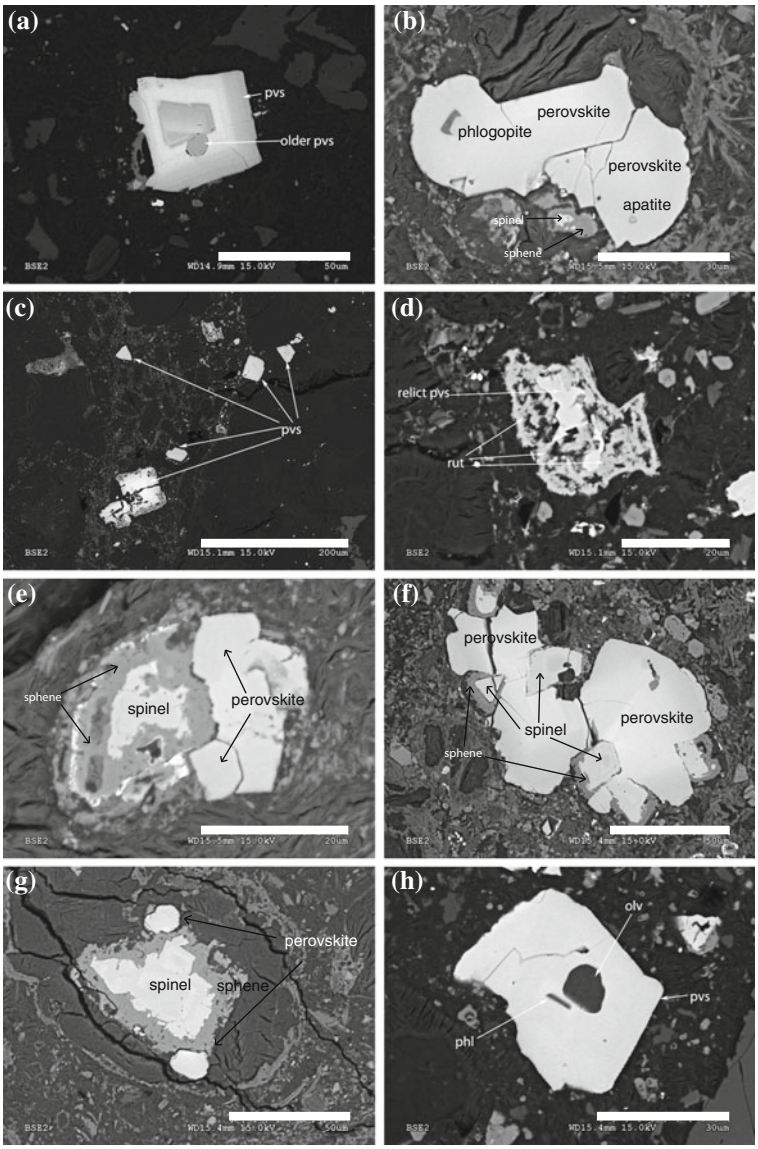


**Fig. 2** Back-scattered electron images of perovskites from Orapa. **a** Euhedral zoned perovskite grain with a core of relict older perovskite. **b** Anhedral perovskite grain with inclusions of phlogopite and apatite. **c** Distribution of fresh unaltered and resorbed perovskite at the hand specimen scale. **d** A perovskite grain with a rim of rutile around it indicating a reaction between perovskite and $CO_2$ to produce the rim of $TiO_2$ around the grain boundary. A small part of the perovskite remains as a relict phase within rutile. **e** Perovskite growing after Fe–Ti spinel, which has reacted to form titanite around its grain boundary. **f** Euhedral spinel with rounded, anhedral perovskite intergrowth. A band of titanite lies between spinel and perovskite. **g** perovskite crystallizing after spinel resorption into titanite. **h** A subhedral perovskite grain with inclusions of serpentinized olivine and phlogopite. (Scale bar is 50 μm in **a**, **f**, **g**; 30 μm in **b**, **h**; 200 μm in **c** and 20 μm in **d**, **e**)

by rutile, although the original shapes are preserved as pseudomorphs. However, the core of the altered grains remains unaffected in case of partial replacement. On the other hand, some perovskite grains appear to be quite resistant and fresh. They often form a lozenge-shaped grains around spinel or olivine or as discrete grains (Fig. 2c, g). All textural varieties were found at variable abundance in each lithofacies of the Orapa kimberlite. However, the pyroclastic kimberlite is dominated by perovskites appearing as discrete groundmass phases. In contrast, volcaniclastic kimberlite contains perovskites appearing mostly as intergrowths with spinel and ilmenite. Both pipes and all lithofacies contain altered and fresh perovskite grains. In fact, the fresh and altered perovskite are so well mixed that almost every thin section studied contains both types of perovskite grains (Fig. 2c).

## Chemical Compositions

Major, minor and trace element compositions of Orapa perovskites are reported in Table 2. Major element compositions of these perovskite grains remain close to ideal $CaTiO_3$ with CaO (36–37.2 wt %), $TiO_2$ (52–54 wt %) and minor amounts of FeO (0.9–1.5 wt %), $Nb_2O_5$ (0.9–1.5 wt %), $Na_2O$ (0.5–0.9 wt %) and REE oxides (6–9 wt %). This range of compositions is very similar to the perovskites reported in kimberlites worldwide (Chakhmouradian and Mitchell 2000, 2001). Niobium and REE are the primary substitutions for Ti while Na replaces Ca for charge balance (Boctor and Boyd 1980, 1981). This is demonstrated by a strong negative correlation of Ca with Na and trace elements (REE, SrO, $Nb_2O_5$ and $ThO_2$; Fig. 3b). Orapa perovskite has low abundance of Na (0.3–1 wt %),

**Table 2** Representative EPMA compositions of perovskite of different textural varieties in Orapa kimberlites

| Sample texture | NP19 | NP19 | NP19 | NP19 | SP1 | SP1 | SP1 | NP1 | NP1 | NP1 |
|---|---|---|---|---|---|---|---|---|---|---|
| *Discrete grain* | | | | | | | | | | |
| Na | 0.55 | 0.52 | 0.71 | 0.55 | 0.48 | 0.68 | 0.59 | 0.49 | 0.58 | 0.52 |
| Mg | – | – | – | – | 0.19 | 0.01 | – | – | 0.01 | – |
| Al | – | – | – | 0.04 | 0.04 | 0.03 | – | – | 0.02 | – |
| Si | – | – | – | – | 0.43 | 0.04 | – | – | 0.03 | – |
| Ca | 25.98 | 25.76 | 24.24 | 25.75 | 25.00 | 24.66 | 25.80 | 26.26 | 25.29 | 26.17 |
| Nd | 0.95 | 0.92 | 1.09 | 1.00 | 0.92 | 1.30 | 0.94 | 0.79 | 0.96 | 0.81 |
| Fe | 0.81 | 0.76 | 0.84 | 0.89 | 1.05 | 0.69 | 0.69 | 0.74 | 0.83 | 0.74 |
| Ti | 32.50 | 31.99 | 31.36 | 32.27 | 33.11 | 31.71 | 32.79 | 31.96 | 32.10 | 32.05 |
| Th | 0.59 | 0.59 | 2.54 | 0.74 | 0.97 | 0.37 | 0.61 | 0.30 | 0.90 | 0.34 |
| Sr | 0.21 | 0.15 | 0.22 | 0.18 | 0.15 | 0.16 | 0.19 | 0.22 | 0.24 | 0.15 |
| Nb | 1.06 | 0.94 | 1.62 | 0.90 | 1.17 | 1.94 | 0.93 | 0.91 | 1.22 | 0.92 |
| Zr | 0.09 | 0.08 | 0.22 | 0.04 | 0.12 | 0.38 | 0.09 | 0.08 | 0.11 | 0.11 |
| Y | – | – | – | – | – | 0.02 | – | 0.01 | 0.03 | 0.02 |
| Pr | 0.17 | 0.11 | 0.23 | 0.17 | 0.18 | 0.28 | 0.14 | 0.19 | 0.20 | 0.21 |
| La | 1.01 | 0.88 | 0.88 | 0.84 | 0.98 | 1.11 | 0.87 | 0.91 | 0.88 | 0.83 |
| Ce | 2.09 | 2.11 | 2.55 | 2.16 | 2.22 | 3.03 | 2.11 | 1.96 | 2.31 | 1.95 |
| Sm | 0.12 | 0.10 | 0.10 | 0.10 | 0.10 | 0.18 | 0.11 | 0.12 | 0.13 | 0.12 |
| O | 33.82 | 33.25 | 33.04 | 33.54 | 33.65 | 33.56 | 33.80 | 33.34 | 33.53 | 33.40 |
| Total | 99.94 | 98.18 | 99.64 | 99.18 | 100.76 | 100.13 | 99.68 | 98.29 | 99.37 | 98.34 |
| Fe/Nb | 0.99 | 1.04 | 0.66 | 1.27 | 1.16 | 0.46 | 0.96 | 1.04 | 0.88 | 1.04 |
| ΔNNO | −1.57 | −1.65 | −3.26 | −0.01 | −2.65 | −6.19 | −2.51 | −1.80 | −1.90 | −1.79 |
| | NP1 | SP7 | SP7 | SP7 | SP7 | NP28 | NP28 | NP28 | NP28 | NP28 |
| *Mantled with spinel* | | | | | | | | | | |
| Na | 0.46 | 0.50 | 0.66 | 0.64 | 0.64 | 0.65 | 0.70 | 0.71 | 0.70 | 0.67 |
| Mg | – | – | – | – | – | – | – | – | – | – |
| Al | 0.01 | – | 0.01 | – | – | – | 0.01 | 0.02 | 0.03 | 0.02 |
| Si | 0.01 | – | – | – | – | – | – | – | – | – |
| Ca | 26.49 | 26.41 | 25.26 | 25.40 | 25.63 | 25.37 | 24.93 | 25.05 | 24.71 | 24.88 |
| Nd | 0.62 | 0.68 | 1.08 | 0.99 | 0.95 | 0.97 | 1.15 | 1.07 | 1.17 | 1.08 |
| Fe | 0.70 | 0.63 | 0.70 | 0.70 | 0.68 | 0.68 | 0.71 | 0.73 | 0.71 | 0.73 |

(continued)

**Table 2** (continued)

| | NP1 | SP7 | SP7 | SP7 | SP7 | NP28 | NP28 | NP28 | NP28 | NP28 |
|---|---|---|---|---|---|---|---|---|---|---|
| Ti | 32.71 | 31.98 | 32.06 | 32.55 | 32.30 | 32.26 | 31.54 | 31.81 | 31.43 | 31.85 |
| Th | 0.01 | 0.06 | 0.87 | 0.75 | 0.64 | 0.77 | 0.49 | 0.85 | 1.43 | 1.35 |
| Sr | 0.18 | 0.19 | 0.17 | 0.15 | 0.24 | 0.20 | 0.21 | 0.19 | 0.20 | 0.17 |
| Nb | 1.29 | 1.33 | 1.30 | 1.25 | 1.48 | 1.43 | 1.83 | 1.53 | 1.59 | 1.46 |
| Zr | 0.31 | 0.23 | 0.17 | 0.22 | 0.20 | 0.21 | 0.27 | 0.26 | 0.21 | 0.20 |
| Y | 0.00 | 0.02 | 0.04 | 0.02 | 0.07 | 0.03 | 0.02 | – | 0.02 | 0.02 |
| Pr | 0.05 | 0.17 | 0.23 | 0.12 | 0.21 | 0.21 | 0.24 | 0.27 | 0.24 | 0.19 |
| La | 0.81 | 0.84 | 1.00 | – | 0.86 | 1.09 | 1.23 | 1.07 | 1.05 | 0.88 |
| Ce | 1.75 | 1.87 | 2.36 | 2.12 | 2.21 | 2.31 | 2.67 | 2.74 | 2.65 | 2.48 |
| Sm | 0.11 | 0.12 | 0.09 | 0.16 | 0.13 | 0.13 | 0.12 | 0.09 | 0.11 | 0.12 |
| O | 34.03 | 33.55 | 33.49 | 33.58 | 33.77 | 33.68 | 33.33 | 33.46 | 33.16 | 33.35 |
| Total | 99.54 | 98.57 | 99.50 | 98.67 | 100.00 | 100.01 | 99.45 | 99.85 | 99.42 | 99.48 |
| Fe/Nb | 0.69 | 0.61 | 0.70 | 0.72 | 0.59 | 0.61 | 0.50 | 0.61 | 0.58 | 0.65 |
| ΔNNO | −3.78 | −4.70 | −3.72 | −3.52 | −4.69 | −4.46 | −5.51 | −4.32 | −4.66 | −3.91 |
| | NP1 | NP1 | NP1 | NP1 | SP1 | SP1 | SP1 | SP1 | NP35 | NP35 |
| *Around olivine* | | | | | | | | | | |
| Na | 0.52 | 0.70 | 0.55 | 0.51 | 0.63 | 0.61 | 0.27 | 0.55 | 0.52 | 0.61 |
| Mg | – | 0.03 | – | – | – | – | – | 0.06 | – | – |
| Al | 0.01 | 0.03 | 0.03 | 0.01 | 0.05 | 0.03 | 0.08 | 0.03 | 0.01 | 0.03 |
| Si | – | 0.08 | – | – | – | – | – | 0.13 | 0.01 | – |
| Ca | 25.68 | 24.51 | 25.89 | 26.21 | 25.58 | 25.53 | 27.41 | 25.56 | 25.98 | 25.77 |
| Nd | 0.98 | 0.95 | 0.91 | 0.81 | 0.91 | 0.99 | 0.45 | 0.97 | 0.92 | 0.96 |
| Fe | 0.76 | 0.84 | 0.79 | 0.71 | 0.89 | 0.81 | 0.92 | 0.79 | 0.76 | 0.84 |
| Ti | 32.71 | 32.67 | 32.69 | 32.52 | 30.93 | 32.05 | 32.61 | 32.18 | 32.56 | 32.09 |
| Th | 0.77 | 1.36 | 0.58 | 0.24 | 0.94 | 0.73 | 0.03 | 0.70 | 0.48 | 0.81 |
| Sr | 0.24 | 0.19 | 0.18 | 0.20 | 0.20 | 0.19 | 0.24 | 0.24 | 0.18 | 0.19 |
| Nb | 0.81 | 1.31 | 0.90 | 0.84 | 1.43 | 1.16 | 1.25 | 0.98 | 0.99 | 1.34 |
| Zr | 0.09 | 0.14 | 0.13 | 0.09 | 0.20 | 0.13 | 0.23 | 0.09 | 0.10 | 0.11 |
| Y | 0.02 | – | – | 0.04 | – | – | 0.01 | – | – | 0.01 |
| Pr | 0.13 | 0.23 | 0.18 | 0.16 | 0.16 | 0.15 | 0.05 | 0.16 | 0.17 | 0.23 |
| La | 0.99 | 0.82 | 0.85 | 0.82 | 1.03 | 0.84 | 0.79 | 0.97 | – | 0.88 |
| Ce | 2.28 | 2.21 | 2.13 | 1.88 | 2.03 | 2.34 | 1.23 | 2.17 | 2.10 | 2.01 |

(continued)

**Table 2** (continued)

| | NP1 | NP1 | NP1 | NP1 | SP1 | SP1 | SP1 | SP1 | NP35 | NP35 |
|---|---|---|---|---|---|---|---|---|---|---|
| Sm | 0.12 | 0.11 | 0.12 | 0.13 | 0.20 | 0.11 | 0.03 | 0.13 | 0.17 | 0.16 |
| O | 33.80 | 33.78 | 33.83 | 33.65 | 32.92 | 33.46 | 34.22 | 33.65 | 33.48 | 33.62 |
| Total | 99.90 | 99.95 | 99.75 | 98.82 | 98.09 | 99.14 | 99.81 | 99.35 | 98.43 | 99.64 |
| Fe/Nb | 1.21 | 0.82 | 1.14 | 1.08 | 0.80 | 0.89 | 0.94 | 1.04 | 0.99 | 0.81 |
| ΔNNO | −1.21 | −2.18 | −1.20 | −1.97 | −1.83 | −1.96 | −1.02 | −2.44 | −2.89 | −3.26 |
| | NP35 | NP35 | NP19 | NP19 | NP19 | NP19 | SP7 | SP7 | SP7 | SP7 |
| *Inclusion* | | | | | | | | | | |
| Na | 0.52 | 0.41 | 0.71 | 0.54 | 0.44 | 0.53 | 0.53 | 0.37 | 0.52 | 0.41 |
| Mg | – | – | – | – | – | – | – | – | – | – |
| Al | – | 0.01 | 0.03 | 0.01 | 0.06 | – | – | 0.03 | 0.01 | 0.01 |
| Si | 0.01 | 0.01 | – | – | – | – | – | 0.02 | – | – |
| Ca | 26.51 | 26.51 | 25.16 | 25.94 | 26.19 | 26.37 | 26.13 | 26.97 | 26.44 | 26.72 |
| Nd | 0.75 | 0.72 | 1.06 | 0.93 | 0.88 | 0.81 | 0.82 | 0.61 | 0.82 | 0.69 |
| Fe | 0.71 | 0.74 | 0.82 | 0.76 | 0.84 | 0.69 | 0.69 | 0.71 | 0.72 | 0.76 |
| Ti | 33.07 | 33.16 | 31.88 | 32.64 | 31.44 | 32.62 | 32.87 | 32.71 | 32.98 | 32.33 |
| Th | 0.23 | 0.12 | 1.54 | 0.51 | 0.50 | 0.14 | 0.26 | – | 0.31 | 0.09 |
| Sr | 0.18 | 0.18 | 0.17 | 0.15 | 0.21 | 0.21 | 0.20 | 0.22 | 0.20 | 0.25 |
| Nb | 0.89 | 0.84 | 0.87 | 0.76 | 0.79 | 0.85 | 0.89 | 0.79 | 0.87 | 0.85 |
| Zr | 0.06 | 0.13 | 0.06 | 0.11 | 0.07 | 0.09 | 0.06 | 0.05 | 0.11 | 0.13 |
| Y | 0.01 | 0.04 | 0.02 | 0.01 | 0.05 | – | – | 0.01 | 0.05 | 0.04 |
| Pr | 0.13 | 0.10 | 0.23 | 0.14 | 0.14 | 0.14 | 0.16 | 0.06 | 0.11 | 0.03 |
| La | 0.73 | 0.80 | 0.97 | 0.98 | 0.86 | 0.82 | 0.91 | 0.61 | 0.75 | 0.74 |
| Ce | 1.96 | 1.90 | 2.58 | 2.29 | 2.04 | 2.00 | 1.97 | 1.55 | 1.97 | 1.59 |
| Sm | 0.11 | 0.09 | 0.11 | 0.17 | 0.13 | 0.13 | 0.13 | 0.11 | 0.10 | 0.10 |
| O | 34.11 | 34.16 | 33.40 | 33.76 | 33.04 | 33.77 | 33.88 | 33.86 | 34.12 | 33.62 |
| Total | 99.99 | 99.92 | 99.61 | 99.69 | 97.66 | 99.17 | 99.51 | 98.68 | 100.06 | 98.37 |
| Fe/Nb | 1.03 | 1.13 | 1.23 | 1.29 | 1.38 | 1.04 | 1.00 | 1.16 | 1.06 | 1.15 |
| ΔNNO | −2.13 | −1.66 | −0.63 | −1.10 | −0.02 | −2.23 | −2.37 | −1.75 | −2.01 | −1.30 |

Elemental abundances are reported in wt%. Analytical uncertainties are 10–15 % (2SD) depending on the concentration

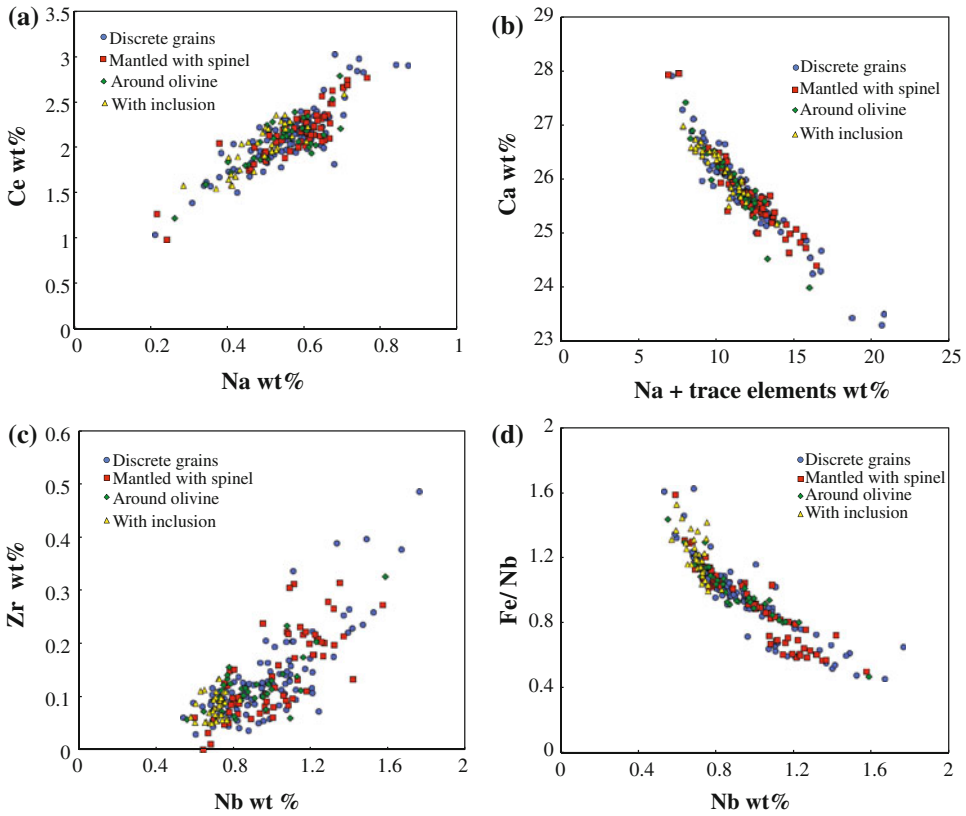


**Fig. 3** Bivariate plot of different varieties of perovskite from Orapa. **a** Ce versus Na showing a positive correlation. **b** Strong negative correlation between Ca and Na + other trace elements. **c** Distribution of Zr and Nb. Note that the perovskite population with inclusions of late-stage minerals (phlogopite ± apatite) has relatively low Zr and Nb contents. **d** Variation of Nb content of perovskite with varying Fe/Nb values

but it has a positive correlation with LREE (especially Ce) content (1–3.5 wt %; Fig. 3a). Perovskites from all lithofacies contain very little $Al_2O_3$ (below detection to 0.3 wt %). In regular zoned perovskite, the core of the grain contains higher LREE, Na and Th while the rim has slightly higher Fe. However, there are no apparent compositional differences between perovskites from different parageneses or from different lithofacies of the Orapa kimberlite. Average major and trace element compositions of perovskites from the North and South Pipes are also similar. Strontium contents of all perovskite grains are remarkably consistent (2,000–2,300 ppm) while Ba appears to be absent (below detection limit). Although certain elements (e.g. Nb, Ta, Zr, Nd, Sm, Th) show some variation, no perovskite was found to be unusually enriched in any element, such as type III perovskite from Lac de Gras area, which have high in Na, Sr, Nb and LREE abundances (Chakhmouradian and Mitchell 2001). Although Fe does not show much variation (0.6–1 wt %), Nb and Zr contents of Orapa perovskites vary considerably (0.5–1.8 and 0.05–0.5 wt %, respectively). Variation of these elements does not correlate with any particular textural type of perovskite. All perovskite grains with inclusions of phlogopite, apatite or those appearing along the grain boundary of resorbed spinel have lower concentrations of Nb, Ta and Zr than other paragenetic varieties (Fig. 3c, d). This group of perovskites stands alone from the rest of the grains as they have low and less variable Nb and Zr contents (0.5–0.7 and 0.05–1.13 wt %, respectively).

Based on the oxybarometer equation given by Bellis and Canil (2007), the oxygen fugacity of the Orapa perovskite was calculated. Overall, the $f(O)_2$ of perovskite ranges between −5.5 and −0.2 with respect to NNO buffer (Fig. 4). The range displayed by discrete groundmass grains, and those that occur as intergrowths with spinel and ilmenite, overlap one another. Perovskites, contained within peletal lapilli or along olivine grain boundaries, record relatively restricted range of $f(O)_2$ (−3.4 to −1.1 NNO). Interestingly, all perovskite grains containing inclusions of phlogopite or apatite and those appearing along the grain boundary of resorbed spinel have relatively high NNO values (−2.3 to −0.2; Fig. 4).

## Discussion

### Crystallization of Perovskite

Petrographic and compositional analyses during this study emphasize the fact that discrete groundmass phase is the major mode of occurrence of perovskite in Orapa kimberlite. Perovskite is a relatively late-crystallizing mineral forming the groundmass. Large nucleation densities produce many small crystals which require elements for growth

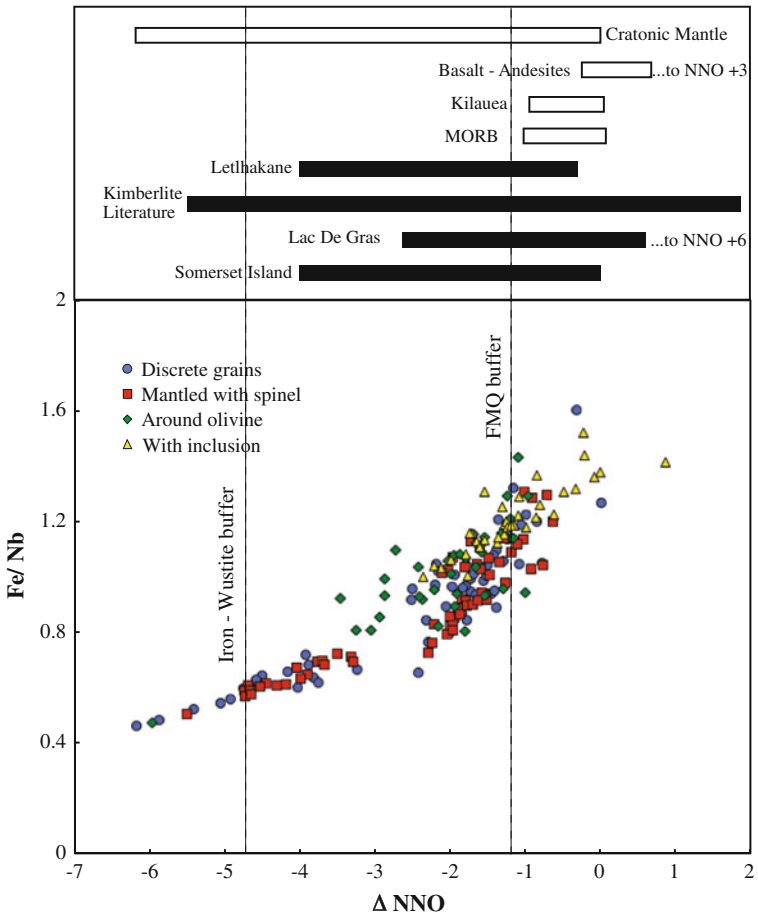


**Fig. 4** Calculated oxygen fugacities (ΔNNO) of different perovskite grains with varying Fe/Nb values. Note that the perovskite population with inclusions of phlogopite ± apatite crystallized from a relatively oxidized magma. Oxygen fugacities (ΔNNO) of global kimberlite bodies, and other mantle-derived magmas are also plotted for reference. $f(O)_2$ ranges of different kimberlites and other magmatic rocks have been taken from Canil and Bellis (2007) while that of Letlhakane has been taken from Trickett (2007). *IW* iron-wustite, *FMQ* fayalite-quartz-magnetite

to be quickly depleted from the melt. It crystallized after most of the macrocrystal phases, such as olivine and Cr spinel, as previously observed by Clement (1982), Mitchell (1986, 2008), Chakhmouradian and Mitchell (2000). Intergrowth of perovskite with Fe–Ti spinel and magnetite suggests simultaneous crystallization (Fig. 1f). Sometimes, perovskite and spinel grew together for a relatively long time period allowing the contact faces to be well preserved (Fig. 1h). The formation of the atoll rim on the spinel occurred at a later stage when the unprotected surface of the grain came into contact with kimberlitic liquid. Sometimes, perovskite preferentially grew by heterogeneous crystallization at pre-existing grain boundaries of olivine, spinel and ilmenite where the activation enthalpy of crystallization was lower. Although it has been reported that perovskite crystallization ceases prior to resorption and development of an atoll rim on these spinels (Mitchell 1986, 2008; Chakhmouradian and Mitchell 2000), petrographic observations of a subset of Orapa perovskite indicate perovskite continues to crystallize during and possibly after the development of atoll rims on spinel. In some places, perovskite grew as a late-crystallizing rim around spinel resorbed into titanite (Fig. 2e, f, g). Titanite is not a primary mineral of kimberlites, and its precipitation indicates some increase in $a_{(SiO_2)}$ during a late evolutionary stage, probably due to contamination of upper crustal material. Although titanite has been reported as an altered phase of perovskite (Mitchell and Chakhmouradian 1998), it only appears to be replacing the spinel phases in Orapa kimberlite (Fig. 2e, f, g). The presence of perovskite rims around resorbed spinel indicates that perovskite crystallization continued at least up to partial resorption of spinel. Inclusions of phlogopite and apatite, which are generally very late-stage minerals in kimberlite (although Malarkey et al. (2010) suggested earlier crystallization of apatite), also support the protracted crystallization history of Orapa perovskite (Fig. 2b, h). Perovskite becomes very unstable during the final evolutionary stages when there is excess $CO_2$ in the system (Mitchell and Chakhmouradian 1998). It then reacts with the $CO_2$-rich fluid to form a $TiO_2$ polymorph (rutile) and calcite that precipitate in the vicinity of perovskite giving a spongy appearance to the assemblage (Fig. 2d). This alteration reaction of perovskite into a $TiO_2$ phase is dependant on temperature and $P_{(CO_2)}$. Nesbitt et al. (1981), Chakhmouradian and Mitchell (2000) have shown that, in the range of reasonable $P_{(CO_2)}$ values, this replacement reaction is confined to relatively low temperatures (<350 °C) and pressures (<2 kbar). However, certain Orapa

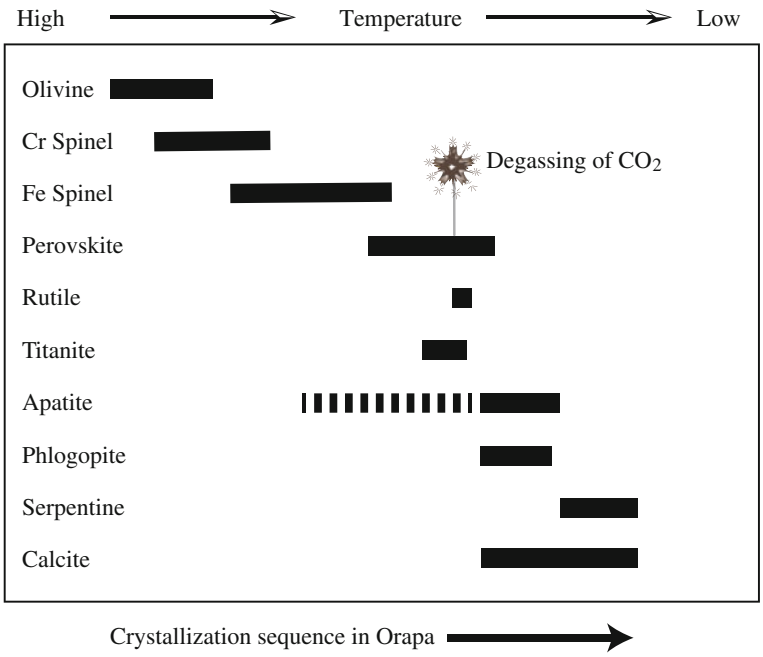


**Fig. 5** Relative crystallization sequence of phenocryst and groundmass minerals (excluding megacrysts/macrocrysts suite) in Orapa kimberlite. The *dashed line* indicates earlier crystallization of apatite as suggested by Malarkey et al. (2010)

perovskite crystals appear to be very fresh and are not converted into rutile, suggesting that they probably did not react with a $CO_2$ fluid (Fig. 2c).

Oxygen isotope data of perovskite from the Orapa kimberlite also suggest a two-stage crystallization (Sarkar et al. 2011). Early-crystallizing perovskites have a mantle-like $\delta^{18}O$ compositions while the second phase of perovskite, which crystallized after degassing, shows very low $\delta^{18}O$ values due to preferential partitioning of $^{18}O$ into the gaseous phase. This two-stage crystallization explains the perovskite alteration pattern nicely. Early-crystallizing perovskites reacted with the $CO_2$ fluid during degassing and precipitated rutile and calcite along their grain boundaries (Fig. 2d), while those crystallizing in post-degassing phase stayed relatively fresh and unaltered as the gaseous phase might have escaped from the system. Minor and trace element concentrations of Orapa perovskite also support this two-stage crystallization model. Abundances of the minor and trace elements in perovskites of different textural types overlap. Nb and Zr are exceptions to this rule; these elements are low in perovskite grains containing inclusions of phlogopite ± apatite or those appearing as a rim around resorbed spinel (Fig. 3c). These textures are indicative of their relatively late crystallization with respect to the other perovskite paragenetic varieties. Low Nb and Zr contents of this textural variety may be attributed to their crystallization after rutile (alteration product of early perovskite), which is a major sink of Nb and Zr. However, it is unclear whether perovskite crystallization paused during degassing as the $\delta^{18}O$ values of the pre- and post-degassing phase perovskite have two distinct clusters (Sarkar et al. 2011). It is unlikely that no perovskite crystallized during rapid degassing accompanying the final stages of kimberlite ascent. Degassing might have a greater impact on oxygen isotope fractionations resulting in two distinctly different clusters, whereas other minor and trace elements generally show a continuum with the late-crystallizing perovskite phase that show limited variability in certain elements (Nb, Zr) due to their preferential partitioning into rutile. The crystallization sequence of Orapa perovskite with respect to other kimberlitic phases is shown in Fig. 5.

## Oxygen Fugacity and Effect of Degassing

The range of oxygen fugacity calculated from Orapa perovskite is NNO −5.5 to NNO −0.2 (Fig. 4). This is consistent with $f(O)_2$ of other kimberlites worldwide (Canil and Bellis 2007; Trickett 2007). It is also evident that kimberlites have the largest range in $f(O)_2$ of all igneous rocks (Carmichael 1991). It has been reported that the oxygen fugacity, shown by perovskite, overlaps with the $f(O)_2$ calculated from groundmass spinel from nearby Letlhakane kimberlite (Trickett 2007). It has also been observed that spinel inclusions in olivine lie towards the more reduced end of the scale (near the iron-wustite buffer) as they grow at a greater depth in the upper mantle and earlier than perovskite. Thus, Orapa perovskite probably started crystallizing under slightly more oxidizing conditions than the IW buffer (∼ −5 NNO) and continued till FMQ (fayalite-magnetite-quartz) buffer (∼ −1 NNO) and beyond (Fig. 4). This interpretation is supported by the calculated $f(O)_2$ values of late-stage Fe–Ti spinel and magnetite, which grow simultaneously with most perovskite

(Trickett 2007; Roeder and Schulze 2008). Some of the highly reduced perovskite grains (lower than IW buffer) probably limit the applicability of this oxygen barometer as it will form metallic iron under such reducing conditions, which is unlikely to be achieved in kimberlite magma. Although there is a degree of overlap, perovskites from different textural parageneses in Orapa show some variability in oxygen fugacity; especially the late-crystallizing ones, which have definitely crystallized from relatively oxidized conditions (−2.3 to −0.2 NNO; Fig. 4). Variability in $f(O)_2$ values shown by Orapa perovskites can be caused by several processes such as degassing, decompression (Carmichael and Ghiorso 1986; Sparks et al. 2006), crystallization (Carmichael and Nicholls 1967) and magma mixing. Bellis and Canil (2007) have argued that early crystallization of olivine and monticellite, which favor $Fe^{+2}$ over $Fe^{+3}$ in their structure, would make the melt increasingly oxidized with progressive crystallization. Thus, the larger range of $f(O)_2$ calculated from Orapa perovskites points towards perovskite crystallization over a wide range of P–T conditions in an evolving kimberlite melt.

Volatile degassing during magma ascent also has a significant impact on the oxidation state of the magma. Sudden degassing of volatiles from a kimberlite magma can trigger large amounts of crystallization (Wyllie and Tuttle 1960; Dalton and Presnall 1998; Dasgupta and Hirschmann 2006; Sparks et al. 2009), which can deplete the melt in ferrous iron, thereby increasing $Fe^{+3}/Fe^{+2}$ ratio in the melt phase (Canil and Bellis 2007). In a volatile-rich rock like kimberlite, various degassing mechanisms involving several gaseous phases would control the oxygen fugacity of the magma. One such mechanism could be the continuous outward degassing of H from the magma, which would dissociate $H_2O$ and increase the O concentration of the magma, thus by increasing the $f(O)_2$ (Carmichael and Ghiorso 1986; Cortés et al. 2006).

$$H_2O_{(m)} \rightarrow H_{2\,(m)} + 1/2O_{2\,(m)} \quad (2)$$

Mathez (1984) has shown that C-rich volatile species would dominate the degassing process. $CO_2$ would be the first vapor species to separate from the melt at shallow pressure. Carbon is dissolved in the magma as $CO_3^{-2}$. On the other hand, solubility of CO and $CO_2$ is independent of the partial pressure of CO and $CO_2$, and the oxidation state of the system (Mathez 1984). Thus, the following two degassing reactions would involve the C species.

$$CO_{3\,(m)}^{-2} \rightarrow CO_{(v)} + O_{(m)}^{-2} + 1/2O_{2\,(m)} \quad (3)$$

$$CO_{3(m)}^{-2} \rightarrow CO_{2(v)} + O_{(m)}^{-2} \quad (4)$$

Reaction (3) produces CO vapor and also increases the O content of the magma, thus oxidizes it, whereas reaction (4) does not involve any change in the oxidation state of the magma. The initial vapor exsolving through reactions (3) and (4) from the magma would be CO rich. Consequently, this will oxidize the melt, and succeeding vapor fractions will be $CO_2$ rich. Gradually, equation (4) would replace (3), and the $f(O)_2$ of the magma will increase slowly. Similar changes to the oxidation state of an ascending magma containing gaseous species including $H_2S$, $S_2$, $SO_2$, $O_2$ and $H_2O$ have been observed by Burgisser and Scaillet (2007). Crystallization of some highly oxidized minerals such as mica and garnet in mela-aillikite has been attributed to exsolution of $CO_2$ gases which has resulted in an increase in $Fe^{+3}$ in the melt (Upton et al. 2006). Another possibility suggested by Ogilvie-Harris et al. (2010) involves monticellite formation from a Ca-rich kimberlite, which releases $CO_2$ while oxidizing the magma. Thus, it can be concluded that several degassing reactions could make the residual magma more oxidized that has been recorded by post-degassing phase perovskite in the form of higher $f(O)_2$ than the early-crystallizing ones (Fig. 4).

## Conclusions

Paragenetic sequence of groundmass minerals varies from one kimberlite to another due to variable magma composition. In Orapa, the chemical composition and textures of perovskites are similar to those reported from other worldwide kimberlites suggesting their crystallization after macrocrystal olivine and Cr spinel but simultaneously with Fe–Ti spinel and magnetite. However, certain petrographic features from Orapa indicate that the perovskite from Orapa kimberlite continued to crystallize until quite late, as they have inclusions of groundmass phlogopite ± apatite and also appear as rims around the Fe–Ti-rich spinel that has reacted to form titanite around its grain boundary. This late-crystallizing perovskite group has lower Nb and Zr abundances indicating their growth after degassing that triggered crystallization of rutile, a sink of Nb and Zr. These perovskite grains also have very low $\delta^{18}O$ values, and they have crystallized from a magma significantly more oxidized than that parental to early formed perovskite.

**Acknowledgements** We are grateful to the anonymous reviewer whose comments have made this manuscript stronger. We thank Steve Sparks, Horst Marschall, Mike Walter and A. P. Jones for their encouragement and important discussions during this project. Stuart Kearns is thanked for his help with the analytical work. We acknowledge De Beers Consolidated Mines and Debswana for giving access to the Orapa mines and samples. This work is part of the PhD research of Chiranjeeb Sarkar, who was funded by the Overseas Research Scholarship and University of Bristol Postgraduate Scholarship along with financial support from De Beers. Chiranjeeb Sarkar is also grateful to the financial assistance provided by the 10th International Kimberlite Conference. CD Storey acknowledges NERC fellowship NE/D008891/2.

## References


Allsopp HA, Bristow JW, Smith CB, Brown R, Gleadow AJW, Kramers JD, Garvie OG (1989) A summary of radiometric dating methods applicable to kimberlites and related rocks. In: Ross J, Jacques AL, Ferguson J, Green DH, O'Reilly SY, Danchin RV, Janse AJA (eds) Kimberlites, Related Rocks., v.1, Proceedings of the fourth international kimberlite conference, Geological Society of Australia Special Publication 14, Perth, Australia, pp 343–357

Armstrong JP, Wilson M, Barnett RL, Nowicki T, Kjarsgaard BA (2004) Mineralogy of primary carbonate-bearing hypabyssal kimberlite, Lac de Gras, Slave Province, Northwest Territories, Canada. Lithos 76:415–433

Batumike JM, Griffin WL, Belousova EA, Pearson NJ, O'reilly SY, Shee SR (2008) LAM-ICPMS U-Pb dating of kimberlitic perovskite: Eocene-Oligocene kimberlites from the Kundelungu Plateau, DR Congo. Earth Planet Sci Lett 267:609–619

Bellis A, Canil D (2007) Ferric iron in $CaTiO_3$ perovskite as an oxygen barometer for kimberlitic magmas I: experimental calibration. J Petrol 48:219–230

Boctor NZ, Boyd FR (1980) Oxide minerals in the Liqhobong Kimberlite, Lesotho. Am Mineral 65:631–638

Boctor NZ, Boyd FR (1981) Oxide minerals in a layered kimberlite-carbonate Sill from Benfontein, South-Africa. Contrib Miner Petrol 76:253–259

Burgisser A, Scaillet B (2007) Redox evolution of a degassing magma rising to the surface. Nature 445:194–197

Canil D, Bellis AJ (2007) Ferric iron in $CaTiO_3$ perovskite as an oxygen barometer for kimberlite magmas II: applications. J Petrol 48:231–252

Carmichael ISE (1991) The redox states of basic and silicic magmas: a reflection of their source regions? Contrib Miner Petrol 106:129–141

Carmichael ISE, Ghiorso MS (1986) Oxidation-reduction relations in basic magma: a case for homogeneous equilibria. Earth Planet Sci Lett 78:200–210

Carmichael ISE, Nicholls J (1967) Iron-titanium oxides and oxygen fugacities in volcanic rocks. J Geophys Res 72:4665–4687

Chakhmouradian AR, Mitchell RH (2000) Occurrence, alteration patterns and compositional variation of perovskite in kimberlites. Can Mineral 38:975–994

Chakhmouradian AR, Mitchell RH (2001) Three compositional varieties of perovskite from kimberlites of the Lac de Gras field (Northwest Territories, Canada). Mineral Mag 65:133–148

Clement C (1982) A comparative geological study of some major kimberlite pipes in the Northern Cape and orange free state. Unpublished Ph.D. thesis, vol 431. University of Cape Town, South Africa

Cortés JA, Wilson M, Condliffe E, Francalanci L (2006) The occurrence of forsterite and highly oxidizing conditions in basaltic lavas from Stromboli volcano, Italy. J Petrol 47:1345–1373

Dalton JA, Presnall DC (1998) The continuum of primary carbonatitic, kimberlitic melt compositions in equilibrium with lherzolite: data from the system CaO, MgO, $Al2O_3$, $SiO_2$, $CO_2$ at 6 GPa. J Petrol 39:1953–1964

Dasgupta R, Hirschmann MM (2006) Melting in the Earth's deep upper mantle caused by carbon dioxide. Nature 440:659–662

Davis GL (1977) The ages and uranium contents of zircons from kimberlites and associated rocks. In: Second international kimberlite conference, Santa Fe, New Mexico (extended abstracts)

Field M, Gibson JG, Wilkes TA, Gababotse J, Khutjwe P (1997) The geology of the Orapa A/K1 kimberlite Botswana: further insight into the emplacement of kimberlite pipes. Geol Geofiz 38:25–41

Field M, Stiefenhofer J, Robey J, Kurszlaukis S (2008) Kimberlite-hosted diamond deposits of southern Africa: a review. Ore Geology Reviews 34:33–75

Gernon TM, Field M, Sparks RSJ (2009) Depositional processes in a kimberlite crater: the upper cretaceous Orapa South Pipe (Botswana). Sedimentology 56:623–643

Gernon TM, Sparks RSJ, Field M (2008) Degassing structures in volcaniclastic kimberlite: examples from southern African kimberlite pipes. J Volcanol Geoth Res 174:186–194

Heaman LM (1989) The nature of the subcontinental mantle from Sr-Nd-Pb isotopic studies on kimberlitic perovskite. Earth Planet Sci Lett 92:323–334

Heaman LM, Kjarsgaard BA, Creaser RA (2003) The timing of kimberlite magmatism in North America: implications for global kimberlite genesis and diamond exploration. Lithos 71:153–184

Heaman LM, Kjarsgaard BA, Creaser RA (2004) The temporal evolution of North American kimberlites. Lithos 76:377–397

Jones AP, Wyllie PJ (1984) Minor elements in perovskite from kimberlites and distribution of the rare-earth elements: an electron-probe study. Earth Planet Sci Lett 69:128–140

Malarkey J, Pearson DG, Kjarsgaard BA, Davidson JP, Nowell GM, Ottley CJ, Stammer J (2010) From source to crust: tracing magmatic evolution in a kimberlite and a melilitite using micros-ample geochemistry. Earth Planet Sci Lett 299:80–90

Mathez E (1984) Influence of degassing on oxidation states of basaltic magmas. Nature 310:371–375

Mitchell RH (1972) Composition of perovskite in kimberlite. Am Mineral 57:1748–1753

Mitchell RH (1986) Kimberlites: mineralogy, geochemistry and petrology. Plenum Press, New York

Mitchell RH (2002) Perovskites: modern and ancient. Almaz Press Ontario, Thunder Bay

Mitchell RH (2008) Petrology of hypabyssal kimberlites: relevance to primary magma compositions. J Volcanol Geoth Res 174:1–8

Mitchell RH, Chakhmouradian AR (1998) Instability of perovskite in a $CO_2$-rich environment: examples from carbonatite and kimberlite. Can Mineral 36:939–951

Nesbitt HW, Bancroft GM, Fyfe WS, Karkhanis SN, Nishijima A (1981) Thermodynamic stability and kinetics of perovskite dissolution. Nature 289:358–362

Ogilvie-Harris R, Field M, Sparks R, Walter M (2010) Perovskite from the Dutoitspan kimberlite, Kimberley, South Africa: implications for magmatic processes. Mineral Mag 73:915

Paton C, Hergt JM, Phillips D, Woodhead JD, Shee SR (2007) New insights into the genesis of Indian kimberlites from the Dharwar Craton via in situ Sr isotope analysis of groundmass perovskite. Geology 35:1011–1014

Roeder PL, Schulze DJ (2008) Crystallization of groundmass spinel in kimberlite. J Petrol 49:1473–1495

Sarkar C, Storey CD, Hawkesworth CJ, Sparks RSJ (2011) Degassing in kimberlite: oxygen isotope ratios in perovskites from explosive and hypabyssal kimberlites. Earth Planet Sci Lett 312:291–299

Sparks R, Brooker R, Field M, Kavanagh J, Schumacher J, Walter M, White J (2009) The nature of erupting kimberlite melts. Lithos 112:429–438

Sparks RSJ, Baker L, Brown RJ, Field M, Schumacher J, Stripp G, Walters A (2006) Dynamical constraints on kimberlite volcanism. J Volcanol Geoth Res 155:18–48

Trickett SK (2007) Mapping lithofacies within the D/K1 kimberlite pipe at Letlhakane, Botswana: an assessment of petrographic, geochemical and mineralogical indicators. PhD Thesis, University College London

Upton B, Craven J, Kirstein L (2006) Crystallisation of mela-aillikites of the Narsaq region, Gardar alkaline province, south Greenland

and relationships to other aillikitic-carbonatitic associations in the province. Lithos 92:300–319

Wu FY, Yang YH, Mitchell RH, Li QL, Yang JH, Zhang YB (2010) In situ U-Pb age determination and Nd isotopic analysis of perovskites from kimberlites in southern Africa and Somerset Island, Canada. Lithos 115:205–222

Wyllie P, Tuttle O (1960) The system CaO, $CO_2$, $H_2O$ and the origin of carbonatites. J Petrol 1:1–46

Yang YH, Wu FY, Wilde SA, Liu XM, Zhang YB, Xie LW, Yang JH (2009) In situ perovskite Sr-Nd isotopic constraints on the petrogenesis of the Ordovician Mengyin kimberlites in the North China Craton. Chem Geol 264:24–42